PAPER

Structural stability and electronic property in K₂S under pressure†

Ying Li, Xilian Jin,* Tian Cui,* Quan Zhuang, Qianqian Lv, Gang Wu, Xing Meng, Kuo Bao, Bingbing Liu and Qiang Zhou

In this work, the structures, phase sequence, and metallic properties of K_2S have been systematically explored. We confirm that the $P6_3/mmc$ phase is the best possible candidate for the stable structure of K_2S at low pressure range. Although the phases of $P6_3/mmc$ and $Cmcm$ K_2S are semiconductors, two new structures of $P6/mmm$ and $P\bar{3}m1$ emerge with metallic characters at high pressures. The analyses of electronic localization functions reveal that the conductivity mainly comes from the electrons surrounding S atom chains, which supplies a potential way to improve the conductivity of sulfur to enhance the electrode recharge ability and rate capability in alkali sulfide battery under pressure.

Introduction

The storage and conversion of energy continue to be important to society. Batteries, which interconvert chemical and electrical energy, are widely used in industry and for consumer applications, *e.g.* appliances and laptop computers. The battery energy storage system, *e.g.* lead-acid battery, solid oxide fuel battery, solar battery, lithium ion battery and so on, are focused and studied for a long time. The lead-acid battery is the most-used battery system with advantages including large current discharge, rechargeable, and low-cost. On the other hand, the disadvantage of lead-acid battery is obvious, for examples, the heavy weight and pollution.[1,2] Solid oxide fuel battery is an energy conversion device that can convert chemical energy directly into electricity without pollution, nevertheless, the high operating temperature limits its widely application in our daily life.[3,4] Solar battery is excepted to have large-scale applications if the problem of low efficiency is solved.[5,6] Lithium ion battery is an attractive battery for the property of portable type, high energy density, and non-pollution, and is widely used for digital products, electric vehicles, household appliances, *etc.*[7–9] The principle of operation lithium ion battery is that Li is removed from an intercalation cathode, for example $LiCoO_2$, on charging and is inserted between sheets of carbon atoms in the graphite negative electrode; discharge reverses this process.[10] Though the compound of Li_2S and Na_2S with high specific energy (energy per unit weight) and energy density (energy per unit volume) are candidates for applications in solid state batteries,[11,12] it is confronted with major challenge, *i.e.*, poor

electrode recharge ability and limited rate capability owing to the insulating nature of sulfur and the solid reduction products.[13]

The ground-state properties of alkali metal sulfides of X_2S (X = Li, Na, K, Rb), *e.g.*, elastic properties, electronic structure, and optical properties are widely studied.[14–17] The calculated band structures show the Li_2S, K_2S, and Rb_2S are indirect bandgap materials, whereas Na_2S is a direct gap material.[14] At the same pressure, bulk modulus of the alkali metal sulfides show a clear decrease with heavier mass of alkali atoms.[15] The similar tendency of decrease with atomic mass of X in X_2S has been also reported on the elastic constants under the same pressure. When the pressure is enhanced, except for the linear decrease of the elastic constant of C_{44}, the bulk modulus and the elastic constant of C_{11}, C_{12} increase in the crystals of Rb_2S, K_2S and Na_2S. Similar trends are also reported in the Li_2S except for the elastic constants C_{44}. It is reported that C_{44} increases linearly with pressure which is related to the difference in the bonding nature of the bottom of the conduction band.[14]

K_2S has been extensively investigated by theoretical and experimental methods since it was first synthesized by Zintl *et al.*[18] It is reported that K_2S can crystallize in the antifluorite structure, *i.e.* $Fm\bar{3}m$[18] at ambient pressure, then transforms to an orthorhombic crystal with the space group of $Pnma$ at about 2.7 GPa.[16] Theoretical prediction points out that $Pnma$ crystal can transform to a distorted $P6_3/mmc$ at 4.4 GPa.[16,19] Nonetheless, the $Pnma$ phase is not observed by experiment to date.[19] In this work, four stable phases of $P6_3/mmc$, $Cmcm$, $P6/mmm$ and $P\bar{3}m1$ have been found at different pressures through *ab initio* ELocR code.[20] The low-pressure phase of $Pmma$ proposed by an experimental analysis[19] is found unstable by our theoretical calculations. Based on the reported X-ray diffraction and our theoretical analysis, we update the low-pressure phase with a hexagonal crystal of $P6_3/mmc$. Our calculations reveal the

State Key Laboratory of Superhard Materials, College of Physics, Jilin University, Changchun 130012, China. E-mail: jinxilian@jlu.edu.cn; cuitian@jlu.edu.cn; Fax: +86-431-85168825; Tel: +86-431-85168825

insulating character of the two phases of $P6_3/mmc$ and $Cmcm$, and the Raman spectra are subsequently analyzed for the experimental convenience. Electronic band structure and the partial density of states show the metallic properties of $P6/mmm$ and $P\bar{3}m1$ at pressures. As shown in the chart of electronic localization functions (ELF), the delocalization of electrons around S atoms in the phases of $P6/mmm$ and $P\bar{3}m1$ denotes the improvement of conductivity of sulfur in Li_2S battery under pressure.

Computational methods

The structural searching of K_2S has been carried out by *ab initio* ELocR code,[20] and the further confirmation with high accuracy of structural relaxations and electronic localization functions (ELF) are completed by the Vienna *ab initio* simulation package (VASP code)[21] with a plan wave cutoff energy of 1000 eV and Brillouin zone sampling grid with a spacing of $2\pi \times 0.04$ Å^{-1}. Total energy calculations are performed using the VASP codes with the Perdew–Burke–Ernzerhof (PBE) parameterization of generalized gradient approximation (GGA)[22] used to treat the exchange–correlation energy. The partial augmented wave (PAW)[23] method is adopted with the PAW potentials where 2s2p and 3s3p4s are treated as valence electrons. The electronic self-consistent calculation is stopped until the energy convergence less than 1×10^{-5} eV.

The electronic projected density of states and the electronic band structure are calculated by CASTEP[24] code with the cutoff energy of 720 eV, GGA-PBE exchange–correlation functional, Brillouin zone sampling grid with a spacing of $2\pi \times 0.03$ Å^{-1}, and norm-conserving pseudopotentials. The Raman spectra are obtained within the density functional theory (DFT) formalism, and PBE exchange–correlation functional with norm-conserving pseudopotentials in the CASTEP code.[25] The dynamical stability properties phonon calculations are carried out by a finite displacement approach[26] through the PHONOPY code.[27] The supercell are: $2 \times 2 \times 2$, $2 \times 2 \times 3$, $2 \times 2 \times 3$, $3 \times 3 \times 3$ for $P6_3/mmc$, $Cmcm$, $P6/mmm$, and $P\bar{3}m1$, respectively. The force constants are calculated from forces on atoms with atomic finite displacements, and the finite displacement size is 0.01 Å in this work.

Results and discussion

We have performed extensive structural searches on K_2S compounds at selected pressures of 0, 50, 100, 150, and 200 GPa. Five phases with lowest enthalpy, *i.e. Fm$\bar{3}$m*, *P6$_3$/mmc*, *Cmcm*, *P6/mmm*, and *P$\bar{3}$m1*, are predicted as presented in Fig. 1. According to our enthalpy curves, the K_2S can crystallize in a face-centered cubic lattice with the space group of *Fm$\bar{3}$m* at ambient pressure, and keep the symmetry up to 3 GPa. The *Fm$\bar{3}$m* phase has been synthesized experimentally at ambient pressure and reported by Zintl *et al.*[18] as shown in Fig. 2(a). The unstable phase *Pmma*[19] is also rebuilt in Fig. 2(b) for the convenience of comparison. Elevating pressure above 3 GPa, a hexagonal phase with *P6$_3$/mmc* symmetry emerges and is stable till 88 GPa, it has been reported by experiment.[28] The
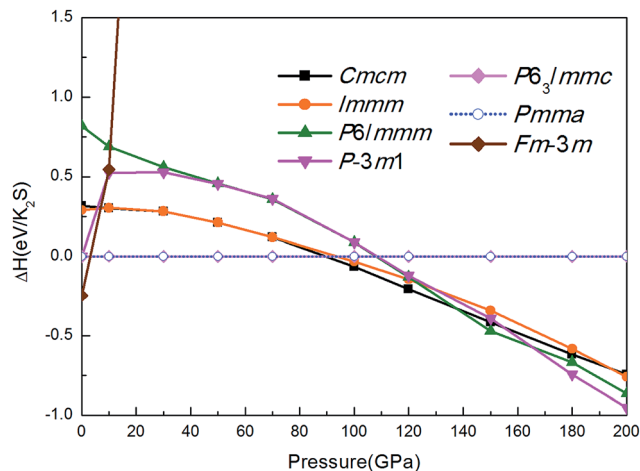

Fig. 1 The calculated enthalpy values per K_2S for various structures relative to previously reported *Pmma*[19] structure as a function of pressure.

layer stacking sequence in the *c*-axis can be denoted by the repeated ABAC stacking. K atoms occupy the crystallographic 2*a* position with $\bar{3}m$ symmetry along *a* axis in A layers, the other nonequivalent K atoms occupy the crystallographic 2*d* position with $\bar{6}m2$ symmetry, locating in B and C layers. S atoms occupy the crystallographic 2*c* position with $\bar{6}m2$ symmetry and locate at C and B positions in B and C layers respectively, as shown in Fig. 2(c). The base-centered orthorhombic phase of *Cmcm* is found with the lowest enthalpy in the pressure range of 88 GPa to 136 GPa, which is about 0.03 eV lower than another body-centered orthorhombic structure of *Immm* per K_2S at 100 GPa. There are two nonequivalent atoms in the crystal lattice, and thus consists of one K_2S unit as shown in Fig. 2(d). K atoms occupy the crystallographic 8*g* position (site symmetry is ..*m*) while S atoms occupy the crystallographic 4*c* position (site symmetry is *m2m*). Each K is surrounding by four S atoms to form a triangular pyramid geometry, and the distance between S and nearest K is 2.492 Å. After 136 GPa, another hexagonal crystal with *P6/mmm* symmetry takes over *Cmcm* phase and becomes most competitive on enthalpy up to 163 GPa. K atoms occupy the crystallographic 2*d* position with $\bar{6}m2$ symmetry, S atoms occupy the crystallographic 1*a* position with $6/mmm$ symmetry. There, K atoms form an interesting graphene-like layered structure in the *ab* plane, and the distance between S and nearest K is 2.590 Å as shown in Fig. 2(e). At high pressure range from 163 GPa to 200 GPa, a trigonal phase of *P$\bar{3}$m1* obtains the minimum enthalpy, which includes two nonequivalent atoms of K and S consisting of layered K–S geometry. The layer stacking sequence in the *c*-axis can be denoted by the repeated ABA stacking. K atoms occupy the crystallographic 2*d* position with 3*m*. symmetry along *b* axis in A layers. S atoms occupy the crystallographic 1*b* position with $\bar{3}m$ symmetry, locating in layers B, as shown in Fig. 2(f). The calculated structural parameters, volume, and Wyckoff positions for each phase are summarized in Table 1.

In order to describe the response of a material to an externally applied stress, the single-crystal elastic constants of
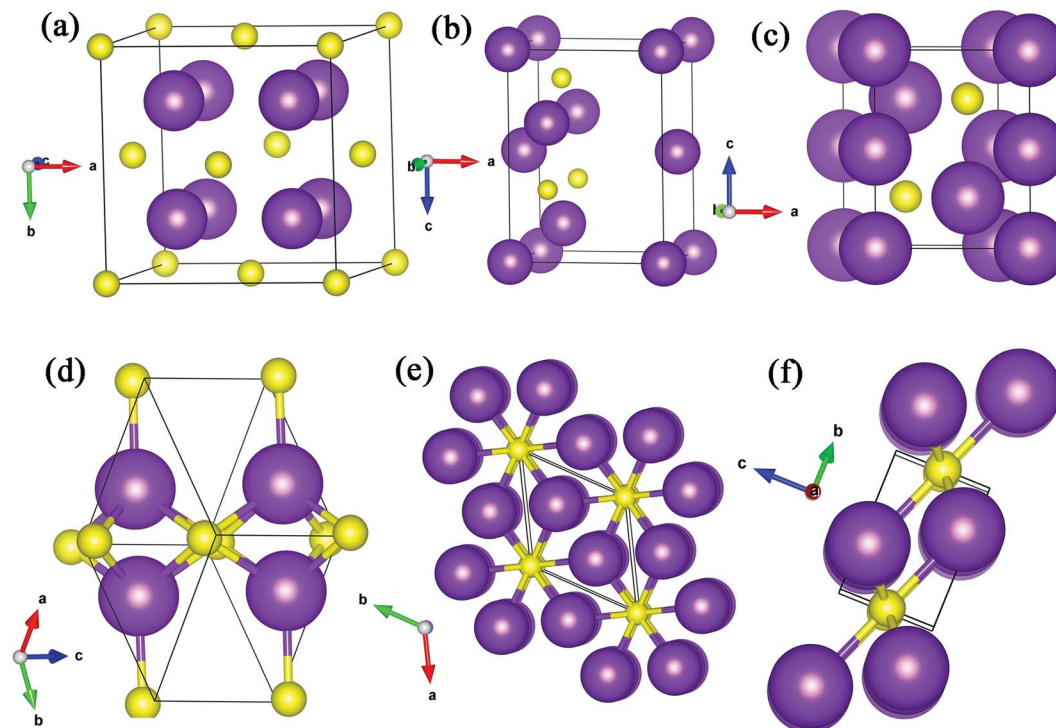
Fig. 2 The structures of K_2S. (a) The $Fm3m$ phase at ambient pressure, (b) the unstable $Pmma$[19] phase at 4.4 GPa, (c) the $P6_3/mmc$ phase at 10 GPa, (d) the $Cmcm$ phase at 100 GPa, (e) the $P6/mmm$ phase at 150 GPa, (f) the $P\bar{3}m1$ phase at 200 GPa. Purple and yellow atoms are K and S, respectively.

Table 1 Structural information of K_2S phases

Space group	Pressure (GPa)	Volume (Å³/K₂S)	Lattice parameter (Å)	Atom (Wyckoff)	Atomic coordinates		
					X	Y	Z
$P6_3/mmc$	10	66.86821	$a = b = 4.9652$	S(2c)	0.33333	0.66667	0.25000
			$c = 6.2634$	K(2a)	1.00000	0.00000	1.00000
				K(2d)	0.33333	0.66667	0.75000
$Cmcm$	100	37.7420125	$a = 7.7793$	S(4c)	0.00000	−0.70000	−0.25000
			$b = 4.4456$	K(8g)	−0.16510	−0.19323	−0.25000
			$c = 4.3653$				
$P6/mmm$	150	32.81625	$a = b = 3.9740$	S(1a)	0.00000	0.00000	0.00000
			$c = 2.3994$	K(2d)	0.33333	0.66667	0.50000
$P\bar{3}m1$	200	29.64067	$a = b = 3.9022$	S(1b)	1.00000	1.00000	−0.50000
			$c = 2.2477$	K(2d)	2.33333	1.66666	−0.90932

proposal structures are calculated and analyzed, as shown in Table 2. The matrix of elastic constants C_{ij} must be positive definite,[29] it is worth noting that negative values are not prohibited for C_{ij}.[30] For hexagonal structure $P6_3/mmc$ and $P6/mmm$, there are five independent elastic constants (C_{11}, C_{12}, C_{13}, C_{33}, and C_{44}), they all satisfy the inequality $C_{44} > 0$, $C_{11} > |C_{12}|$, $(C_{11} + 2C_{12})C_{33} > 2C_{13}^2$, it confirms that $P6_3/mmc$ and $P6/mmm$ are mechanically stable. As to orthorhombic structure $Cmcm$, independent elastic constants C_{22}, C_{33}, C_{44}, C_{55}, C_{66}, C_{12}, C_{13}, and C_{23} meet the inequality $C_{11} > 0$, $C_{22} > 0$, $C_{33} > 0$, $C_{11} + C_{22} + C_{33} + [2(C_{12} + C_{13} + C_{23})] > 0$, $(C_{11} + C_{22} - 2C_{13}) > 0$, $C_{44} > 0$, $C_{55} > 0$, $C_{66} > 0$, $(C_{22} + C_{33} - 2C_{23}) > 0$, which conforms mechanical stability of $Cmcm$ at corresponding pressure range. $P\bar{3}m1$ belongs to trigonal system, the independent elastic constants

also satisfy the inequality $C_{44} > 0$, $C_{11} > |C_{12}|$, $(C_{11} + 2C_{12})C_{33} > 2C_{13}^2$, indicating the mechanical stability of $P\bar{3}m1$. So, the proposal structures all satisfy Born–Huang criterion,[31] representing the stability of the mechanical property.

The mechanically and thermodynamically stability of proposal phases have been discussed, and they are all stable at relevant pressure range. Furthermore, the phonon band structure and partial phonon density of states (PHDOS) for atoms with nonequivalent Wyckoff positions are calculated to judge its dynamical stability as shown in Fig. 3, and the absence of imaginary frequency modes in the entire Brillouin zone indicates dynamic stability of the structures. From the PHDOS on nonequivalent atoms in $P6_3/mmc$ crystal at 50 GPa as plotted in Fig. 3(a), we can see clearly that the low frequency modes mainly

Table 2 The calculated elastic constant C_{ij} (GPa) of $P6_3/mmc$, $Cmcm$, $P6/mmm$, $P\bar{3}m1$ at 10, 100, 150, and 200 GPa, respectively

Space group	C_{11}	C_{12}	C_{13}	C_{33}	
	C_{22}	C_{23}	C_{55}	C_{66}	C_{44}
$P6_3/mmc$	101.19881	43.82810	20.79056	114.65024	22.52524
	101.19881	20.79056	22.52524	28.68536	
$Cmcm$	568.50040	245.86790	170.10752	465.26990	27.42380
	545.48660	134.70090	108.92205	107.29615	
$P6/mmm$	786.32800	412.58015	276.12338	585.58230	149.94920
	786.32800	276.12338	149.94920	186.87393	
$P\bar{3}m1$	905.68978	124.02977	100.68456	966.62216	307.39376
	124.02977	100.68456	307.39376	390.83000	

dominated by the K atoms occupying the crystallographic $2a$ position, but the other nonequivalent K atoms occupying the crystallographic $2d$ position contribute more than K atoms with $2a$ position at high frequency modes. In the $Cmcm$ phase, S atoms mainly contribute to the frequency upon 14 THz while the low frequency below 14 THz mainly comes from the vibrations of K atoms at 100 GPa, see the Fig. 3(b). At higher pressure range from 150 GPa to 200 GPa, there are no distinguishing characteristics in $P6/mmm$ and $P\bar{3}m1$ K$_2$S except K atoms contribute more than S atoms as a whole because the number of K atoms is twice the number of S atoms in K$_2$S crystals as shown in Fig. 3 (c) and (d).

There is a discussion needed with the proposal phase in low pressure range. Experiment proposes a crystal with the space group of $Pmma$[19] at 4.4 GPa, which is not consistent with the structure of $P6_3/mmc$ proposed in this work. We rebuild $Pmma$

phase according to the space group and atomic coordinates given by the experiment report, and calculate the phonon dispersion and elastic constants. The matrix of elastic constants C_{ij} are as shown in ESI,† which contains $C_{11} < 0$, $C_{55} < 0$, $C_{66} < 0$, $C_{11} + C_{22} - 2C_{12} < 0$, $C_{11} + C_{33} - 2C_{13} < 0$. For the orthorhombic structure, elastic constants do not satisfy Born–Huang criterion,[31] representing the instability of the mechanical property. Phonon band structure is added in ESI.† There are imaginary frequency modes in the entire Brillouin zone indicates dynamic instability of the structures. Comparing the experimental X-ray powder diffractograms as shown in Fig. 4(a) and (c), the peak position and intensity of $P6_3/mmc$ K$_2$S coincide well with reported experiment observation. So, the reported $Pmma$ structure is unstable theoretically, and the $P6_3/mmc$ phase is the best possible candidate for the stable structure of K$_2$S at low pressure range.

Moreover, Raman spectroscopies of $P6_3/mmc$ and $Cmcm$ are simulated and display in Fig. 4(b) and (d). The Raman spectroscopy of $P6_3/mmc$ can be classified by the irreducible representation of the point group D_{6h}, a weak characteristic peak is observed at 96 cm^{-1} correspond to E$_{2g}$, the another peak appear at 196 cm^{-1} also belong to E$_{2g}$ irreducible representation. $Cmcm$ vibrational modes belong to the D_{3h} point group, the peaks at 82 cm^{-1}, 442 cm^{-1} and 519 cm^{-1} are related to A$_g$ irreducible representation, the peaks at 253 cm^{-1}, 341 cm^{-1} and 484 cm^{-1} are correlated with B$_{1g}$. The following peaks at 255 cm^{-1} and 551 cm^{-1} are connected with B$_{3g}$, the positions of the peak at 337 cm^{-1} is corresponding to B$_{2g}$. The two close peaks at 253 cm^{-1} and 255 cm^{-1} produce an intense peak, and the other two
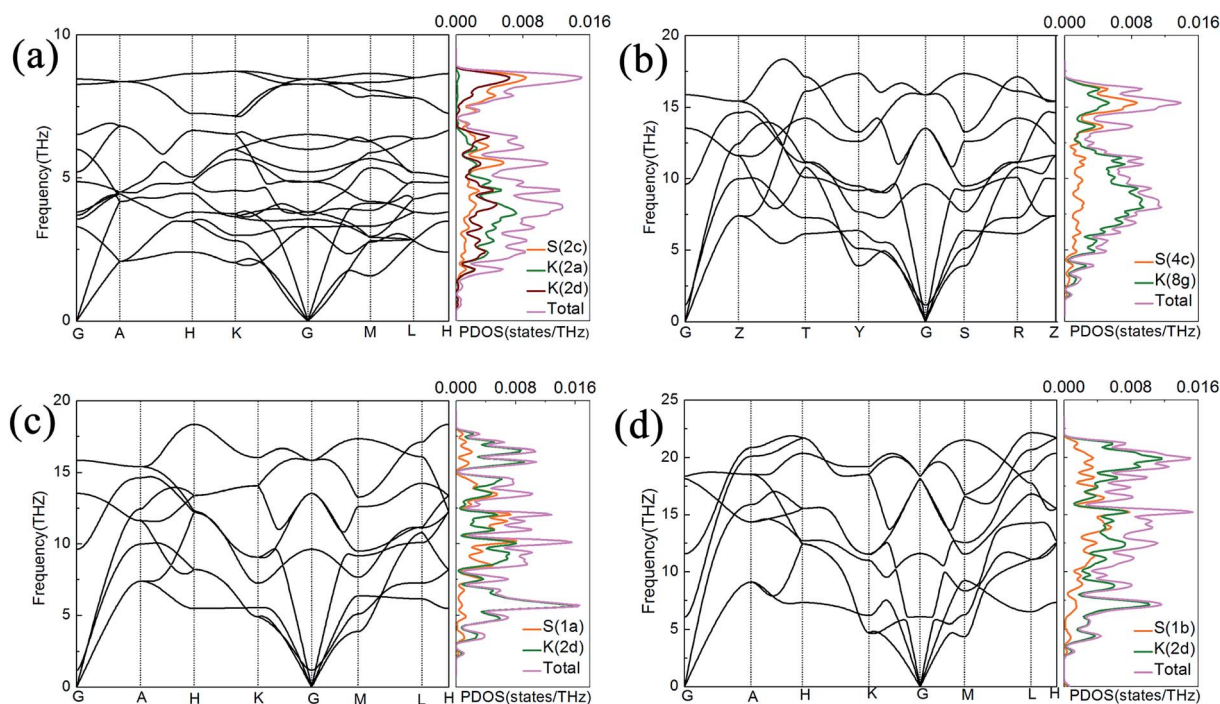
Fig. 3 The phonon band structure and partial phonon density of states for atoms with nonequivalent Wyckoff positions are plotted for the proposal phases. (a) $P6_3/mmc$ phase at 50 GPa, (b) $Cmcm$ phase at 100 GPa, (c) $P6/mmm$ phase at 150 GPa, (d) $P\bar{3}m1$ phase at 200 GPa, respectively.
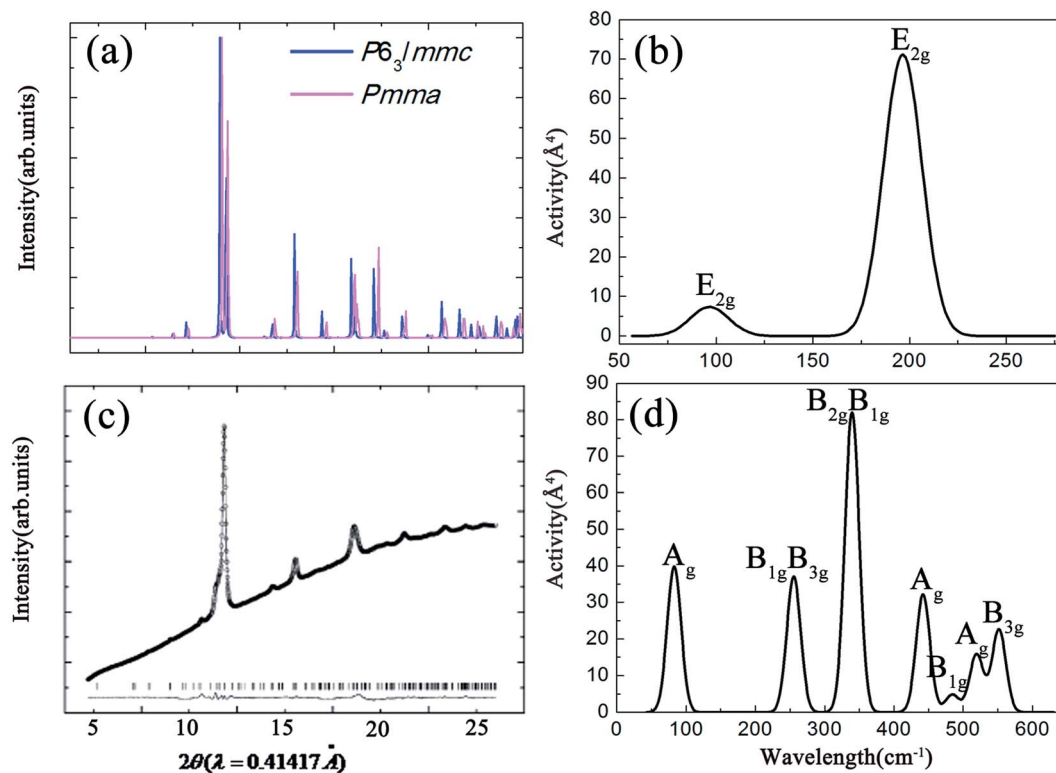
Fig. 4 (a) Calculated difference X-ray power diffraction for $P6_3/mmc$ and $Pmma$ which is rebuilt though data from experiment at 4.4 GPa, (b) Raman active modes of $P6_3/mmc$ phase, (c) experiment X-ray power diffraction for $Pmma$ at 4.4 GPa,[19] (d) Raman active modes of $Cmcm$ phase.

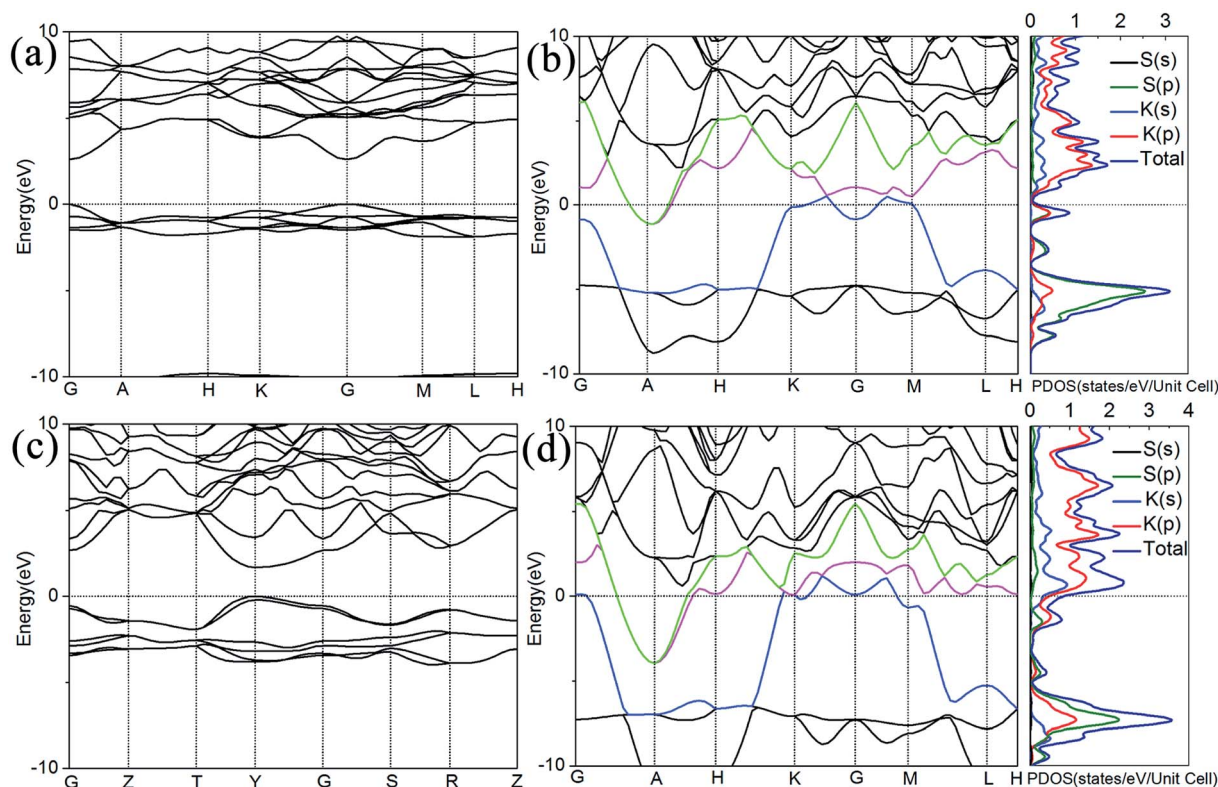

Fig. 5 The electronic band structure and PDOS of K_2S. (a) The electronic band structure of $P6_3/mmc$, (b) the electronic band structure and PDOS of $P6/mmm$, (c) the electronic band structure of $Cmcm$, (d) the electronic band structure and PDOS of $P\bar{3}m1$.

close peaks at 337 cm^{-1} and 341 cm^{-1} combine the most intense peak.

In order to analyze the electronic properties of phases $P6_3/mmc$, $Cmcm$, $P6/mmm$, and $P\bar{3}m1$, the electronic band structure and the partial density of states are further explored in Fig. 5. Band gap is discovered in the $P6_3/mmc$ phase at 50 GPa, revealing the nonmetallic character which coincides with previously report.[14] The electronic band structure of $Cmcm$ phase shows the semiconductor character, as displayed in Fig. 5(c). The band gap decreases with pressure from $P6_3/mmc$ to $Cmcm$ by contrast to the values of gaps at 50 GPa and 100 GPa in Fig. 5, respectively. Elevating the pressure to 150 GPa, three bands marked with magenta, green, and blue crossing over the Fermi level contribute large total electronic density distribution, and revel the strong metallic character of $P6/mmm$, as displayed in Fig. 5(b). Three bands intersecting the Fermi level, the $P\bar{3}m1$ phase also behaves as a metal, and the bands colored by blue and magenta closing to Fermi level are found to contribute more to the density of states (DOS) of Fermi level, as displayed in Fig. 5(d). From the partial density of states (PDOS) in Fig. 5(b) and (d), the metallic character of $P6/mmm$ and $P\bar{3}m1$ is confirmed by the high level of total electronic density distribution at Fermi level. The majority of occupied states come from K(p) state, whereas the contribution from K(s), S(s) and S(p) to the states around the Fermi level is quite small.
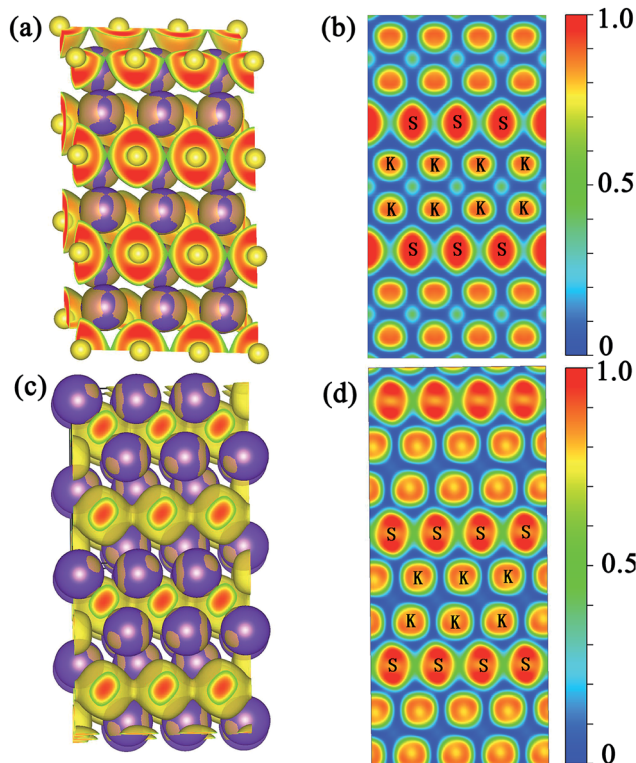
The electronic localization functions (ELF) is derived from an earlier idea of Lennard-Jones[32] and first reported by A. D. Becke and K. E. Edgecombe.[33] It has been calculated to characterize the degree of electron localization in the proposal K$_2$S crystals. ELF as defined runs from 0 to 1, the values of ELF equaling to 1.0 and 0.5 reflect the extremely strong localization and homogeneous electrons distribution, respectively.[33,34] Three-dimensional electron location function (3D ELF) of $P6/mmm$ and $P\bar{3}m1$ show free-electron channels with isosurface value of 0.5 (ELF = 0.5) around S atoms, which reveals that the conductivity comes from the contributions of the electrons around the S atoms as presented in Fig. 6(a) and (c). Furthermore, the two-dimensional electron location function (2D ELF) confirm the character of conductivity in two crystals, where connected regions with the ELF equaling to 0.5 are surrounding S atoms as shown in Fig. 6(b) and (d). Potassium is an alkali element and always described as a typical free-electron-like metal at ambient pressure; on the contrary, sulfur is often described as a good insulator at the same condition. Nevertheless, free electrons assemble around only S atom chains demonstrating the conductivity, and not K atoms under high pressure. At ambient pressure, K$_2$S is crystallized in face-centered cubic antifluorite structure with $Fm\bar{3}m$ symmetry which is an ionic crystal[14] and performed insulator characters. Nevertheless, the two phases of $P6/mmm$ and $P\bar{3}m1$ exhibit metallic features as discussed above, which implies the available improvement of the conductivity of sulfur to enhance the electrode recharge ability and rate capability in alkali sulfide battery under pressure.

Conclusion

In summary, we have systematically explored phase sequence of K$_2$S at pressures from ambient pressure to 200 GPa using the *ab initio* ELocR, and stable structures of $Fm\bar{3}m$, $P6_3/mmc$, $Cmcm$, $P6/mmm$, and $P\bar{3}m1$ have been explored thoroughly. Based on enthalpies, phonon band structure, elastic constants, and X-ray power diffraction, we confirm that the reported $Pmma$ structure is unstable and can distort into $P6_3/mmc$ by our calculations. Moreover, we also simulate the Raman spectroscopies of $P6_3/mmc$ and $Cmcm$ phases for the convenience of the further studies of experiments. The two phases of $P6_3/mmc$ and $Cmcm$ K$_2$S are semiconductors under pressure, $P6/mmm$ and $P\bar{3}m1$ emerge with the nature of metallic characters at higher pressures. The analyses of ELF show that the conductivity comes from the electrons surrounding S atom chains, which implies the potential improvement of the conductivity of sulfur to enhance the electrode recharge ability and rate capability in alkali sulfide battery under pressure.

Fig. 6 Electron localization function of $P6/mmm$ and $P\bar{3}m1$ phase. (a) $P6/mmm$ 3D electron localization function (3D ELF) map with the ELF values of 0.5, (b) $P6/mmm$ 2D electron location function (2D ELF) slice along the (110) plane, (c) $P\bar{3}m1$ 3D electron localization function (3D ELF) map with the ELF values of 0.5, (d) $P\bar{3}m1$ 2D electron location function (2D ELF) slice along the (010) plane.

Acknowledgements

Development Program of Science and Technology of Jilin Province, China (No. 20150312002ZG). Parts of calculations were performed in the High Performance Computing Center (HPCC) of Jilin University.

References

1 H. Bode, *Lead-acid batteries*, John Wiley, New York, 1977.

2 Z. M. Salameh, M. A. Casacca and W. A. Lynch, *IEEE Transactions on Energy Conversion*, 1992, **7**, 93–98.

3 S. C. Singhal, *Solid State Ionics*, 2000, **135**, 305–313.

4 N. Q. Minh, *Solid State Ionics*, 2004, **174**, 271–277.

5 W. Shockley and H. J. Queisser, *J. Appl. Phys.*, 1961, **32**, 510.

6 M. A. Green, K. Emery and Y. Hishikawa, *Prog. Photovoltaics*, 2015, **23**, 1–9.

7 L. Gao, S. Liu and R. A. Dougal, *IEEE Trans. Compon. Packag. Technol.*, 2002, **25**, 495–505.

8 Y. Idota, T. Kubota and A. Matsufuji, *Science*, 1997, **276**, 1395–1397.

9 J. O. Besenhard, J. Yang and M. Winter, *J. Power Sources*, 1997, **68**, 87–90.

10 P. G. Bruce, L. J. Hardwick and K. M. Abraham, *MRS Bull.*, 2011, **36**, 506–512.

11 P. G. Bruce, S. A. Freunberger and L. J. Hardwick, *Nat. Mater.*, 2012, **11**, 19–29.

12 H. Momida, T. Yamashita and T. Oguchi, *J. Phys. Soc. Jpn.*, 2014, **83**, 124713.

13 Y. J. Choi, K. W. Kim and H. J. Ahn, *J. Alloys Compd.*, 2008, **449**, 313–316.

14 H. Khachai, R. Khenata and A. Bouhemadou, *Solid State Commun.*, 2008, **147**, 178–182.

15 R. D. Eithiraj, G. Jaiganesh and G. Kalpana, *Phys. Status Solidi*, 2007, **244**, 1337–1346.

16 J. C. Schön, Ž. Čančarević and M. Jansen, *J. Chem. Phys.*, 2004, **121**, 2289.

17 H. Khachai, R. Khenata and A. Bouhemadou, *J. Phys.*, 2009, **21**, 095404.

18 E. Zintl, A. Harder and B. Dauth, *Z. Elektrochem. Angew. Phys. Chem.*, 1934, **40**, 588–593.

19 A. Vegas, A. Grzechnik and M. Hanfland, *Solid State Sci.*, 2002, **4**, 1077–1081.

20 A code for crystal structural prediction and analysis is based on evolutional local random computational method, and is developed by our group. Some details have been provided in ESI.†

21 G. Kresse and J. Fürthmuller, *Phys. Rev. B: Condens. Matter Mater. Phys.*, 1996, **54**, 11169–11186.

22 J. P. Perdew, K. Burke and M. Ernzerhof, *Phys. Rev. Lett.*, 1997, **77**, 3865–3868.

23 P. E. Blöchl, *Phys. Rev. B: Condens. Matter Mater. Phys.*, 1994, **50**, 17953–17979.

24 S. J. Clark, M. D. Segall and C. J. Pickard, *Crystalline Materials*, 2005, **220**, 567–570.

25 M. D. Segall, P. J. D. Lindan and M. J. Probert, *J. Phys.: Condens. Matter*, 2002, **14**, 2717–2744.

26 K. Parlinski, Z. Q. Li and Y. Kawazoe, *Phys. Rev. Lett.*, 1997, **78**, 4063–4066.

27 A. Togo, F. Oba and I. Tanaka, *Phys. Rev. B: Condens. Matter Mater. Phys.*, 2008, **78**, 134106.

28 H. F. Fischmeister, *Monatsh. Chem.*, 1962, **93**, 420–434.

29 J. F. Nye, *Physical Properties of Crystal*, Oxford Univ. Press, Oxford, 1985, pp. 142–143.

30 J. P. Perdew and K. Burke, *Phys. Rev. Lett.*, 1997, **77**, 3865–3868.

31 Z. Wu, E. Zhao and H. Xiang, *Phys. Rev. B: Condens. Matter Mater. Phys.*, 2007, **76**, 054115.

32 J. E. J. Lennard-Jones, *Chem. Phys.*, 1952, **20**, 1024.

33 A. D. Becke and K. E. Edgecombe, *J. Chem. Phys.*, 1990, **92**, 5397–5403.

34 J. K. Burdett and T. A. McCormick, *J. Phys. Chem. A*, 1998, **102**, 6366–6372.